The 9th European Congress on Computational Methods in Applied Sciences and Engineering
ECCOMAS Congress 2024
3–7 June 2024, Lisboa, Portugal

# IDENTIFICATION OF LOSSES FROM ENGINE-AIRFRAME INTERACTION FOR A PASSENGER AIRCRAFT THROUGH INTEGRATED SIMULATION

**JAN MUELLER[1], KAZUHISA CHIBA[1] AND YOSHINORI OBA[2]**

[1] The University of Electro-Communications (UEC)
Graduate School of Informatics and Engineering
1-5-1 Chofugaoka, Chofu, Tokyo 182-8585, Japan
e-mail: ma004016@edu.cc.uec.ac.jp, kazchiba@uec.ac.jp

[2] IHI Corporation
Aero Engine, Space & Defense Business Area
3975-18 Haijima, Akishima, Tokyo 196-8686, Japan
email: oba1132@ihi-g.com

**Key words:** Computational Fluid Dynamics, Finite Volume Method, Transsonic Flow, Turbomachinery

**Summary.** In this study, we conducted an integrated analysis of an aircraft airframe and operating engines in cruise flight. We present different approaches that have either proven beneficial or detrimental to simulation stability and discuss the method we used to achieve physically plausible results. Further, we conducted an analysis of the flow around the fan, throughout the engine nacelle (bypass duct) as well as around the fuselage. Through a comparison between the integrated case and a simulation of the airframe with flow-through nacelles, we were able to identify interaction effects between the engine spill flow, the flow around the wings, and the engine exhaust that have a negative impact on drag, lift and thrust.

## 1 INTRODUCTION

In the civil aviation industry, we see an ever increasing demand for more environmentally friendly transport solutions. These demands can be met in a variety of ways from improved wing and fuselage designs to completely new propulsion methods. While many of these solutions show merit, their maturation and integration into existing aviation infrastructure will take considerable time. For achieving greener aviation in the near future, a significant effort is put into increasing the fuel efficiency of current jet engines. - This is usually achieved by larger fans and therefore a higher engine bypass ratio. However, the increased engine size poses its own problems in integration with the aircraft frame:

If larger engines are mounted onto an aircraft on conventional under-wing pylons, it will be difficult to maintain ground clearance. This would require a larger landing gear, which could lead to structural issues and may also cause incompatibility with current airport infrastructure. Furthermore, thrust from these lower mounted engines would be applied through a longer pitch moment arm, which could negatively impact flight behaviour.

On the other hand, mounting the engines higher, would mean placing parts of the engine nacelle in front of the wing leading edge, where the nacelle wake could impact the flight behaviour.

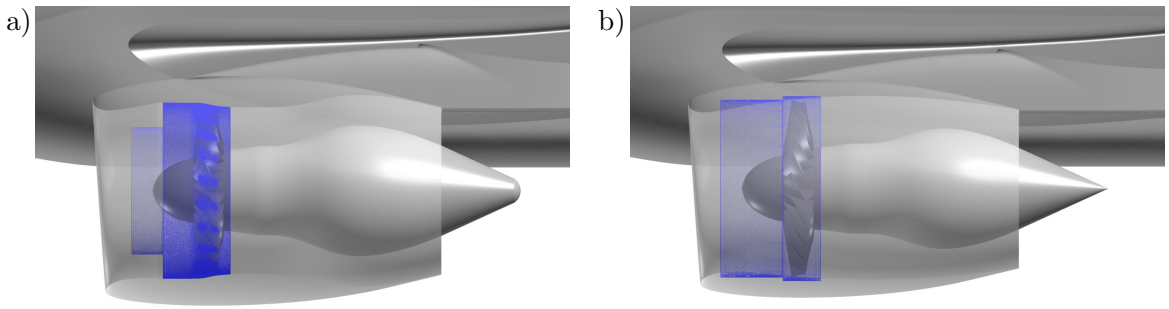


**Figure 1**: Nacelle geometry with the rotating domain marked in blue. In a) for the current sliding-mesh simulations, in b) for previous overset-mesh simulations.

In addition, the exhaust jet would now also run closer to the wing underside which could lead to further unwanted interactions. These interactions need to be understood to design an efficient aircraft and engine combination. However, at the current time, it is difficult to predict such interactions early in development. An important factor here is, that aircraft and engine design are treated as completely separate processes: Engines are tested standalone or are simulated with pre-computed input parameters. Aircraft model experiments and simulations are usually performed with flow-through nacelles or preset engine inflow and outflow conditions. Unwanted interactions between engine and airframe can only be identified late in development, when both components are integrated.

A simulation of the integrated aircraft with engine would allow us to catch these interactions early enough in the development process, that they could be taken into account and the design could be adapted accordingly, leading to a better optimized and therefore more efficient aircraft. Individual simulations of engines or airframes are already complex and resource intensive by themselves. Therefore, it is important to start simple and confirm the feasibility of an integrated simulation first, before more complexity is added. Further, it is desirable to identify any interaction phenomena that appear in our integrated simulations.

## 2 SIMULATION PARAMETERS

We start with simple geometries to identify which tools and settings are required to achieve a stable integrated simulation. Once the simulation works reliably, we can step by step add complexity in future research. Therefore, our current simulation setup is based on well-researched geometries: For the airframe, we use the model of the NASA Common Research Model (CRM) from AIAA's Sixth Drag Prediction Workshop [1] in cruise configuration, consisting of **w**ing, aircraft **b**ody, engine **n**acelle and engine **p**ylon (wbnp). We altered the model by tilting the nacelle so its central axis is oriented parallel to the roll axis of the aircraft. Further, we altered the inside of the flow-through nacelle geometry to form an adequate bypass shroud geometry. To this, we added an additional rear passage, which forms the hub of the bypass duct geometry as seen in Figure 1a). - Bypass hub and shroud geometries were provided by the IHI corporation.

In an integrated simulation with airframe, a full engine simulation would be too complex. Therefore, the engine is represented by only the fan stage, without any stator or engine core. For the fan rotor, we utilize NASA Rotor67, as very detailed experimental reference data is available in [2]. The rotor has 22 blades and we run it at its design speed of $\omega_{fan} = 16,043\,\mathrm{rpm}$. The

rotor is modeled at 1:1 scale, with the CRM shrunk down to fit the nacelle around the rotor. This leaves the airframe at a length of $l_{CRM} = 9.584\,\mathrm{m}$.

### 2.1 Simulation Method

Simulations are carried out with JAXA's FaSTAR Move AE [3], a compressible finite volume method (FV) solver for three-dimensional unstructured meshes. Computation is based on the Reynolds-averaged-Navier-Stokes equations, solved by a cell-centered MUSCL-scheme with the simple low dissipation advection upstream scheme [4] for numerical flux calculations. Turbulence is computed with the one equation Spalart-Allmaras model. Simulations are carried out as stationary, with the spinning fan represented as frozen rotor. Even for stationary computations, FaSTAR Move AE employs some time dependent terms, these are handled through the lower-upper symmetric Gauss-Seidel (LU-SGS) implicit method [5]. Simulations are initially started without a slope limiter (first order spatial accuracy), but once the simulation has converged, we employ Hishida's differentiable slope limiter [6] to re-compute the result with second order spatial accuracy (see also Section 3.6). Fan blades, spinner and rotor shroud are bundled into the rotating domain - marked blue in Figure 1a), which interfaces with both the nacelle diffuser and the nozzle through the sliding mesh method.

### 2.2 Simulation Setup

The computations are performed for the cruise conditions of the NASA CRM at a mach number of $M = 0.85$ and an angle of attack $\alpha = 2.75°$ with no sideslip angle $\beta = 0°$, which allows us to use a half-span model of the aircraft. An additional simulation is performed for $\alpha = 5.0°$ to deduce the lift characteristic of the integrated aircraft. Flight conditions are based on flight level 180 (5486.4 m) in the international standard atmosphere (ISA), with boundary conditions pressure $p_{\mathrm{inf}} = 50606\,\mathrm{Pa}$ and temperature $T_{\mathrm{inf}} = 252.49\,\mathrm{K}$. These were selected to achieve a total temperature at the fan inlet of $T_{t,in} \approx 288.15\,\mathrm{K}$ to match the reduced engine speed in our simulation with the NASA reference data. The farfield boundary is modeled as a hemisphere with a diameter of $d_{\mathrm{inf}} = 25 \cdot l_{CRM}$, to avoid any boundary effects close to the aircraft.

Additionally, we performed reference simulations without a rotor ("flow-through" nacelle) and without rotor, nacelle and pylon ("no nacelle"). Geometries were discretized with an unstructured tetrahedral mesh and 45 prism layers at the walls to resolve boundary layer flows. The mesh count for all domains is presented in Table 1. Computations were carried out on a three-node laboratory cluster (20-core Intel Xeon E5-2670v2 @ 2.5 GHz, 256 GB memory per node). The computational mesh is divided by METIS [7] and assigned to each core.

Convergence was judged based on the histories of the lift- ($C_L$) and drag coefficients ($C_D$) as shown in Figure 2a) and b) respectively, as well as the residual shown in Figure 2c). Once we could not observe any further changes in the coefficient histories we considered a simulation as converged. All simulations were started without a slope limiter, but after converging (usually after 60,000 steps) the simulation would be continued with active slope limiter for increased accuracy results.

**Table 1**: Mesh element count for the performed simulations.

| | integrated (airframe) | integrated (rotor) | flow-through | no nacelle |
|---|---|---|---|---|
| Nodes | 59,015,715 | 110,846,111 | 79,862,870 | 30,748,703 |
| Total Elements | 165,485,981 | 307,159,446 | 228,068,648 | 87,053,156 |
| Tets | 73,647,457 | 133,059,328 | 105,406,649 | 39,538,313 |
| Pyramids | 227,208 | 2,206,747 | 353,237 | 90,616 |
| Prisms | 91,611,316 | 171,893,371 | 122,308,762 | 47,424,227 |

## 3 TESTED METHODS

Before arriving at the simulation method presented in Section 2, we explored several other ways to set up our simulation. We would like to briefly present the most relevant of these tested methods here and discuss why they proved inadequate for our specific simulations.

### 3.1 Overset Mesh Method

In previous simulations [8], we employed the overset-mesh method to realize the rotation of the fan. As shown in Figure 1b), the rotating domain encompasses a high resolution mesh around the fan blades, rotor hub and spinner. In the stationary domain, the volume occupied by the rotor is discretized as a coarse "background" mesh, without any of the rotating boundaries. The rotor geometry is manifested in the static domain through a hole-cutting process and flow data is exchanged between overlapping volumes. An advantage of the overset mesh method is that thanks to this hole cutting, the geometries do not have to be matched exactly: The rotor shroud does not have to be separately modeled in the rotating domain and the rotor can simply be placed into the passage of the CRM flow-through nacelle (see Section 3.2).

However, performing the hole-cutting process for every time-step required a significant amount of CPU time. Further, the overset-mesh method in FaSTAR was only implemented for transient (time evolution) simulations which by default require more computational resources. Coupled with a low CFL-number ($CFL = 5 \cdot 10^{-4}$) to run a stable computation and the inability to generate a stationary initial condition based on a running rotor, our overset mesh simulations would not reach sufficient convergence even after one year of runtime [9].

### 3.2 Simplified Geometry

As stated in Section 2, the complex engine geometry has to be simplified for efficient integrated simulation but physical phenomena still need to be represented with sufficient accuracy. The geometry for the overset-mesh simulations was built by fitting the rotor (and nozzle hub) directly inside the flow-through nacelle of the CRM as seen in Figure 1b). In conjunction with the slow convergence of the overset-mesh simulations, this shroud geometry would prevent the formation of a proper engine exhaust jet and therefore no interactions between exhaust and wing flow could be observed. The switch to the sliding-mesh method required the inclusion of a rotationally symmetric rotor shroud in the rotating domain (and further downstream in the nozzle), which we based on the NASA Rotor 67 shroud geometry [2] and additional data provided by the IHI Corporation. With this matched shroud geometry we observe proper jet formation, so

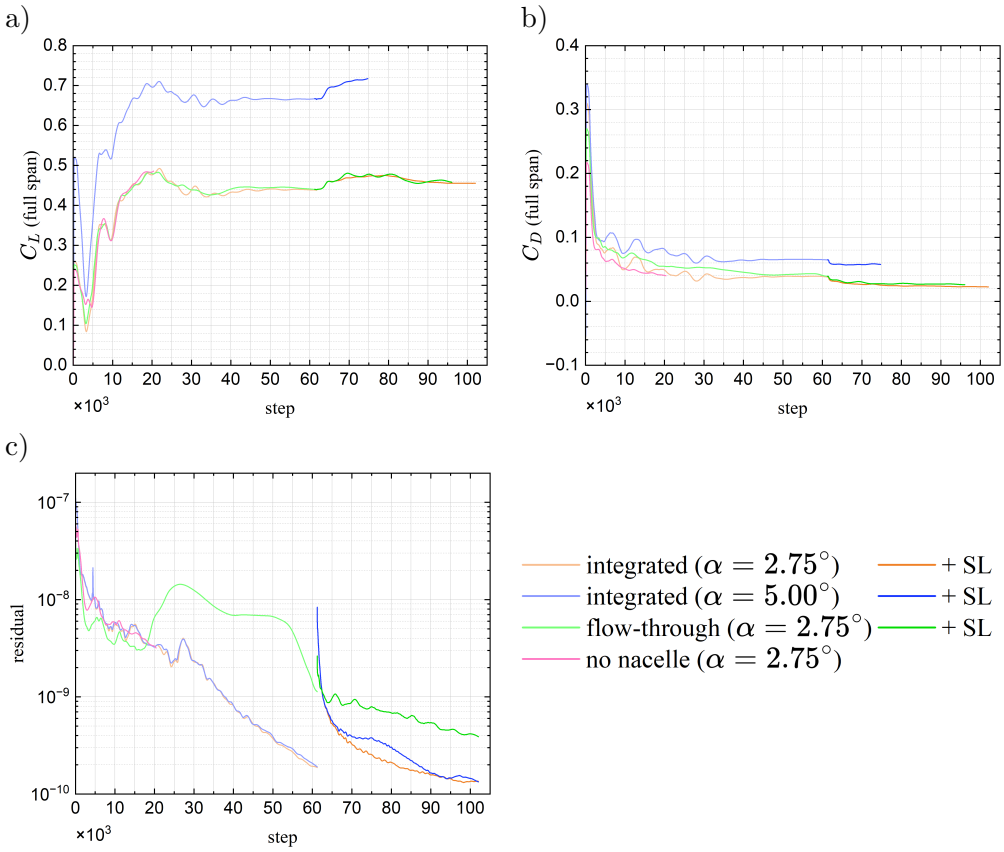


**Figure 2**: Coefficient histories a) for lift coefficient, b) for drag coefficient and c) residual history for the performed simulations. Once a simulation without slope limiter has sufficiently converged, it is continued with active slope limiter (+SL) for better accuracy.

interactions with the exhaust can now be analyzed.

### 3.3 Cell-Vertex FV

For simulations that demand high accuracy for the computation of boundary forces, the cell-vertex FV is generally preferred [10]. In FaStar / FaSTAR Move, this is available for stationary domains and overset-mesh method simulations. The sliding-mesh based solver FaSTAR Move AE only supports cell-centered FV, so we are limited to this scheme for our current integrated simulations. However, tests with stationary geometries (flow-through nacelle) show no significant differences in the $C_D$ and $C_L$ histories between either scheme.

### 3.4 Mesh Refinements

Especially in regions of steep flow gradients such as near the rotor blades, a sufficient mesh resolution is imperative. This is not only true for the rotor surface mesh, but also for the prism layers that resolve the boundary layer flow. Early meshes of the rotor blade surface had patterns of quickly alternating mesh resolution at the leading and trailing edges. When generating a volume mesh with MEGG3D, these patterns would translate into variable amounts

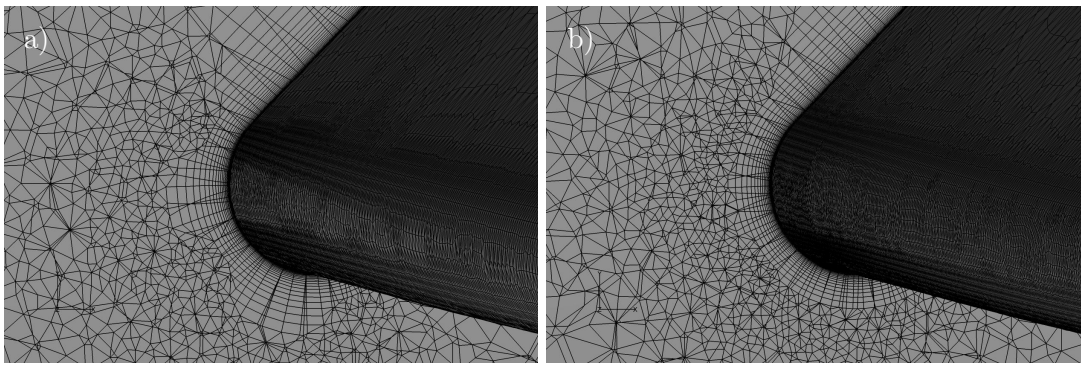


**Figure 3**: In a), low quality prism layers form if the mesh resolution at the boundary surface (here the fan blade leading edge) alternates too rapidly. A smooth surface mesh as in b) results in more continuous prism layers

of prism layers placed on top as seen in Figure 3a). The pyramid elements placed in these layer transitions would often be the cause of locking. Through a smoothing of the mesh resolution on the blade edge surfaces, we could enforce the generation of more consistent prism layers as seen in Figure 3a) which enables a much more stable simulation.

### 3.5 CFL-Number

Even for stationary computations, FaSTAR still retains time dependent terms in the governing equations it employs. This means, even stationary (and frozen-rotor) simulations can be characterized with a Courant-Friedrichs-Levy number (CFL-number). FaSTAR and its related solvers are based on implicit FV schemes, so there is no strict requirement for CFL $\leq 1$ to achieve a stable simulation. However, a lower CFL number could still be considered more stable/accurate in exchange for longer computation times. Early sliding mesh simulations were performed at CFL = 0.5 [9], as these would initially run stable (without slope limiter), but would lock after about 10,000 steps shortly before reaching sufficient convergence. Further reduction if the CFL-number would only drag out the process over an increased amount of timesteps, but lead to the same lockup.

Thanks to improvements in the surface mesh quality (see Section 3.4), new simulations could now be started with CFL = 100 without immediately locking. We found these simulations to run more stable than the previous CFL = 0.5 simulations and they would converge without crashing. In return, we found that the evolution of the $C_D$ and $C_L$ histories (and therefore the speed towards convergence) was slowed down by about a factor of four (see Figure 4). This does not only mean increased computation times, but it is also counter-intuitive to how the CFL-number usually affects computations. Our assumption is, that the fluctuations in the coefficient histories are related to the computation scheme itself and not to any physical processes that would scale with the CFL-number. In turn, the increased CFL-number may dampen out any high-frequency physical oscillations that peviously would have introduced enough noise into the system to lock the simulation.

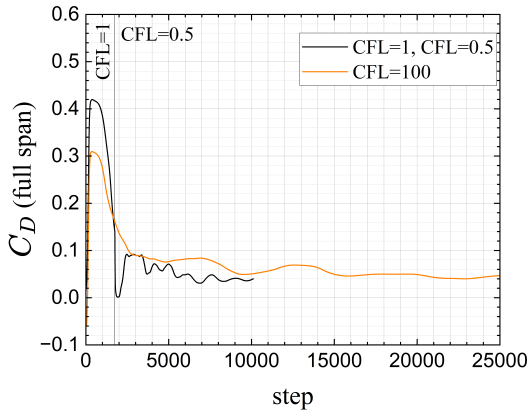


**Figure 4**: Evolution of the drag coefficient for different CFL-numbers. After the initial spike, we still observe similar oscillation behaviour. However, for the CFL = 100 simulation, the oscillations are stretched out over about four times as many timesteps.

### 3.6 Slope Limiter

A slope limiter is generally employed to improve FV simulation stability and accuracy. However, we found that an active slope limiter may introduce a significant stability penalty at the start of a simulation. Initial suspicions, that this penalty is dependent on the selection of the cell-vertex or cell-centered scheme could not be corroborated in later tests and the dependency appears to be primarily related to the geometry (including mesh resolution) and the CFL-number. Initial sliding-mesh simulations would lock after about 30 steps when started with an active slope limiter of any kind. Therefore, simulations would be first started without a slope limiter and only after sufficient convergence has been reached (after about 60,000 steps), the Hishida (van Leer) [6] slope limiter is turned on. The penalty introduced by the slope limiter still upsets the simulation, seen as a jump in the residual in Figure 2c) but is not so severe as to lock the simulation.

## 4 RESULTS

At the time of writing, not all simulations have yet reached convergence. Therefore, this discussion will mostly focus on data without slope limiter unless otherwise noted.

### 4.1 Rotor Flow

The integrated simulation provides detailed data on the flow around the rotor blades. Figure 5 shows cuts through the blade geometry at positions similar to the ones that were experimentally surveyed in [2]. Our results for the flow field are very similar to the NASA data near the blade leading edge. On the other hand, our simulation shows shocks between the blades for $\eta_r = 70\%$ and $\eta_r = 90\%$ sitting directly at the blade trailing edge, whereas they are positioned further upstream in the experiments. The shock for $\eta_r = 30\%$ is not even present in the experiments.

A look at the engine characteristic in Figure 6 explains the discrepancy: The rotor is choked. While we were able to match the inflow conditions of the rotor to the experimental data, the nozzle geometry is completely different and designed to be used in conjunction with a stator

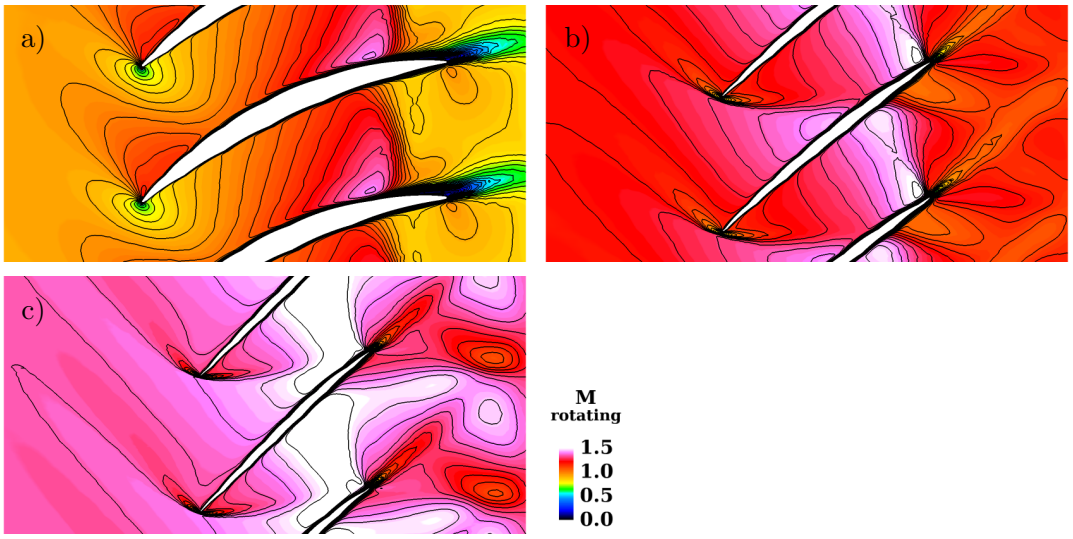


**Figure 5**: Mach number in the rotating frame of reference around the fan blades for the integrated simulation without slope limiter. With a) 30% from hub, b) 70% from hub and c) 90% from hub.

behind the fan rotor. This lack of counter-pressure causes the rotor to let through an increased corrected mass flow ($\dot{m}_{corr}$), dropping the pressure ratio ($\Pi$) and the efficiency ($\eta$) in turn.

As the total temperature at the rotor inlet is slightly changing over the course of the simulation, the individual operation ponts in Figure 6 exist on different curves of constant corrected engine speed. Therefore, they do not align perfectly with the experimental data curve.

While we could verify a satisfying representation of the rotor inflow, the outflow conditions are too different from the experimental case to draw a full comparison. This further means that the engine flow is insufficiently converted into thrust, leading to an underpowered exhaust jet. Adjustments to the nozzle geometry or the inclusion of a stator to adjust the rotor outflow pressure would be desirable, but have to be weighed against the increased computational effort.

### 4.2 Nacelle Flow

Figure 7 shows the flow field throughout the nacelle. For the integrated simulation, we can clearly observe an exhaust jet in the Mach number ($M$) plot. In the pressure coefficient ($Cp$) plot, we can further observe low pressure regions, which are the vortex cores of the jets (the angular momentum is not converted by a stator). Inside the nacelle, we can also observe shock waves running off from the rotor, which are especially prominent in the results with slope limiter.

In the $M$ plot, the larger supersonic areas around the nacelle inlet reveal an increased spill flow for the integrated simulations. This matches the different mass flow rates shown in Figure 8, where the flow-through nacelle can channel a much higher mass flow as the integrated simulation.

Further, we observe a low pressure region behind the pylon, that is much more pronounced in the integrated simulations, where it even reaches into the exhaust vortex core. In the $M$ plot, we can observe the jet curving upwards after passing this low pressure area. The change in angle is larger than $\alpha = 2.75°$ and therefore can not solely be caused by the sourrounding flow.

Finally, for the result with slope limiter, the high velocity area on the top side of the wing is significantly more pronounced, but the shock is moved noticeably forward.

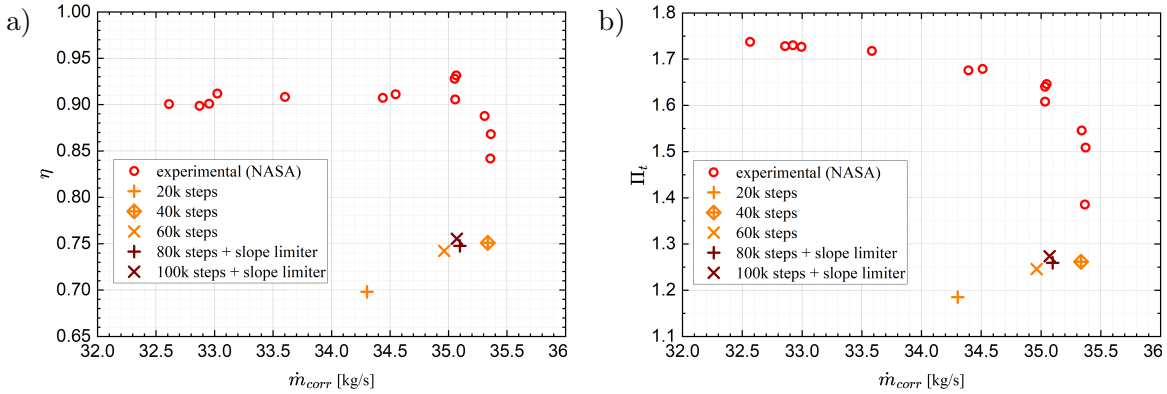


**Figure 6**: Engine characteristic for the integrated simulation at different steps in the computation. With a) representing fan efficiency and b) fan pressure ratio.

### 4.3 Wing Pressure Distribution

Figure 9 compares the wing pressure distributions for the flow-through nacelle (without slope limiter) with the integrated simulation (with and without slope limiter). On the wing top side, the distributions appear overall very similar, but for the integrated simulations, the pressure differences are more pronounced. We can also observe the shock shifted forward for the slope limiter result.

On the wing underside, the integrated simulation results show much more pronounced low pressure areas. We can observe the formation of a supersonic shock around the pylon near the low pressure area discussed in Section 4.2. The low pressure (supersonic) area between fuselage and nacelle is a lot more pronounced in the integrated simulations and in the simulation with slope limiter even terminates in a shock.

### 4.4 Interaction Mechanism

From the above results, we were able to deduce a chain of interactions that alter the flow around the wing based on the presence of the running engine. When housing an engine, the nacelle can not take in as much air as a flow-through nacelle would. (The choked engine does in fact present the least impactful case here, as it provides the maximum mass flow for a given engine speed.) This increases the spill-flow which has to be channeled around the outside of the nacelle. Any spill-flow that gets diverted towards the fuselage is now boxed in by fuselage, wing underside and nacelle. The geometry acts like a de Laval nozzle and accelerates the flow to supersonic speeds, creating strong low pressure areas on the wing underside that negatively impact lift. The additional shocks formed at the end of the supersonic areas also increase the drag. Finally, the exhaust jet is affected by these low pressure areas and bent upwards and towards the fuselage which affects thrust.

## 5 CONCLUSIONS

We were able to perform a stable integrated simulation of aircraft and running engine. However, simplifications were necessary and the current computation does not have a fan stator or considers the engine core in any way.

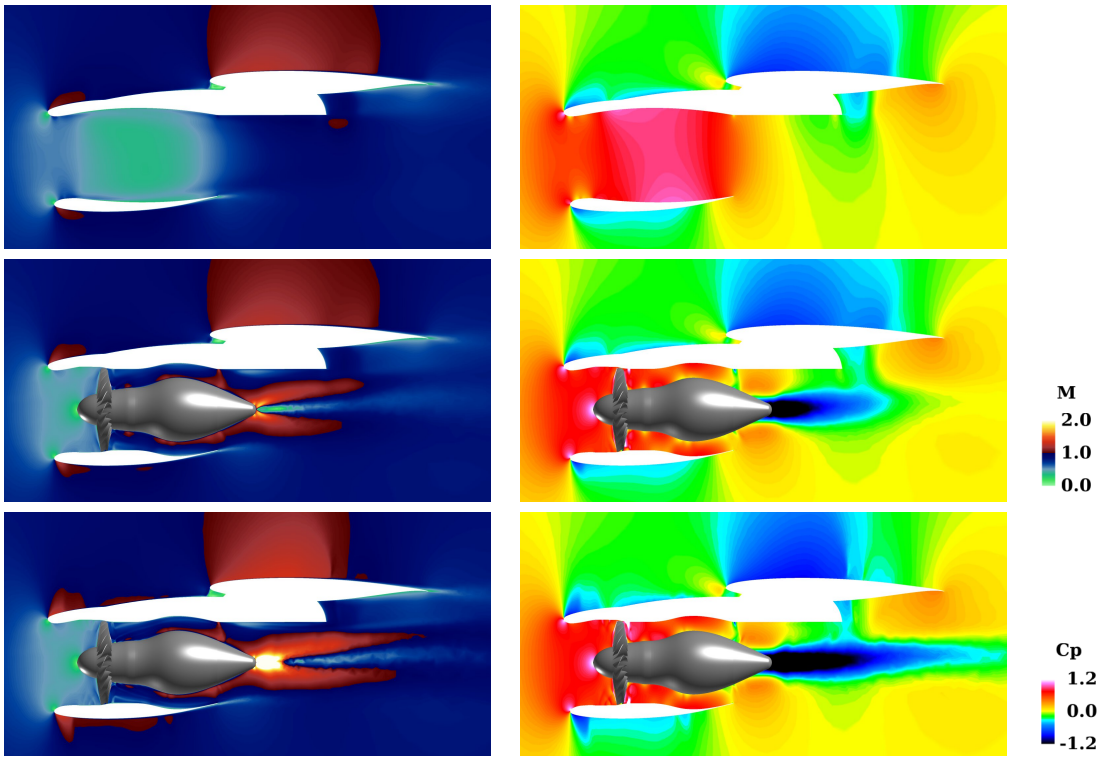


**Figure 7**: Flow in a vertical cut along the rotor axis. Mach number $M$ on the left and pressure coefficient $Cp$ on the right. Datasets from top to bottom are flow-through nacelle without slope limiter, integrated simuation without slope limiter and integrated simulation with slope limiter.

Further, we were able to verify that the presence of an engine indeed impacts the aircraft aerodynamics: Larger supersonic regions at the wing underside reduce lift with the terminating shocks adding additional wave drag, whereas the deflection of the exhaust jets reduces the thrust. We also noted that the corrected engine speed is highly susceptible to slight changes at the rotor inflow, which confirms that the exact engine behaviour is hard to predict in isolated engine simulations where the inflow conditions are more stable. Therefore, we can conclude that an integrated simulation is meaningful to simulate interaction effects between aircraft and engine that otherwise could not be identified during development.

With future simulations it would be desirable to compare different operational states (e.g. cruise at a higher altitude, near-stall, takeoff, etc.). We would also like to introduce a reference simulation without engine, nacelle or pylon. To measure the impact of higher bypass ratio engines, a simulation with a larger nacelle (and engine) relative to the airframe size would also be desirable. Finally, the introduction of further complexity, such as a stator, flaps, or the switch to a transient simulation could be considered depending on the available computational resources.

## 6 ACKNOWLEDGEMENTS

This paper is based on results obtained from project JPNP20010, commissioned by the New Energy and Industrial Technology Development Organization (NEDO).

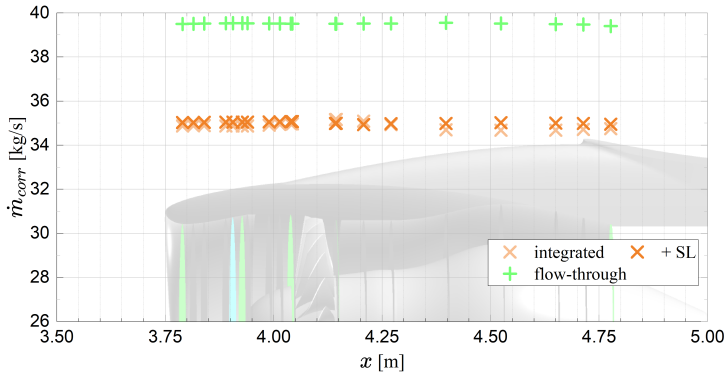


**Figure 8**: Mass flow distribution throughout the engine nacelle for the integrated and flow-through simulations.

## REFERENCES

[1] E. N. Tinoco, O. P. Brodersen, and S. Keye et al. Summary data from the sixth AIAA CFD drag prediction workshop: CRM cases. *Journal of Aircraft*, 55(4):1352–1379, 2018.

[2] A. J. Strazisar, J. R. Wood, M. D. Hathaway, and K. L. Suder. Laser anemometer measurements in a transonic axial-flow fan rotor. NASA TP-2879, 1989.

[3] R. Steijl and G. Barakos. Sliding mesh algorithm for CFD analysis of helicopter rotor-fuselage aerodynamics. *International Journal for Numerical Methods in Fluids*, 58:527–549, 2008.

[4] K. Kitamura and E. Shima. Towards shock-stable and accurate hypersonic heating computations: A new pressure flux for AUSM-family schemes. *Journal of Computational Physics*, 245:62–83, 2013.

[5] D. Sharov and K. Nakahashi. Reordering of hybrid unstructured grids for Lower-Upper Symmetric Gauss-Seidel computations. *AIAA Journal*, 36(3):484–486, 1998.

[6] M. Hishida, A. Hashimoto, K. Murakami, and T. Aoyama. New slope limiter function for fast unstructured CFD solver FaSTAR. JAXA-SP-10-012, 2010 (in Japanese).

[7] G. Karypis and V. Kumar. METIS: A software package for partitioning unstructured graphs, paritioning meshes, and computing fill-reducing orderings of sparse matrices. Technical Report 97-061, University of Minnesota, 1997.

[8] H. Ishikawa, K. Chiba, and Y. Oba. Numerical study of nasa rotor 67 under running conditions on an unstructured hybrid mesh. In *Aerospace Europe Conference*. 3AF, 2020.

[9] J. Mueller, K. Chiba, and Y. Oba. Influence of the engine exhaust on the wing pressure distribution, computed with an integrated simulation of airframe and running engine. In *AIAA Aviation 2023 Forum*. AIAA, 2023.

[10] G. Wang, A. Schwoppe, and R. Heinrich. Comparison and evaluation of cell-centered and cell-vertex discretization in the unstructured tau-code for turbulent viscous flows. In *ECCOMAS CFD*. CIMNE, 2010.

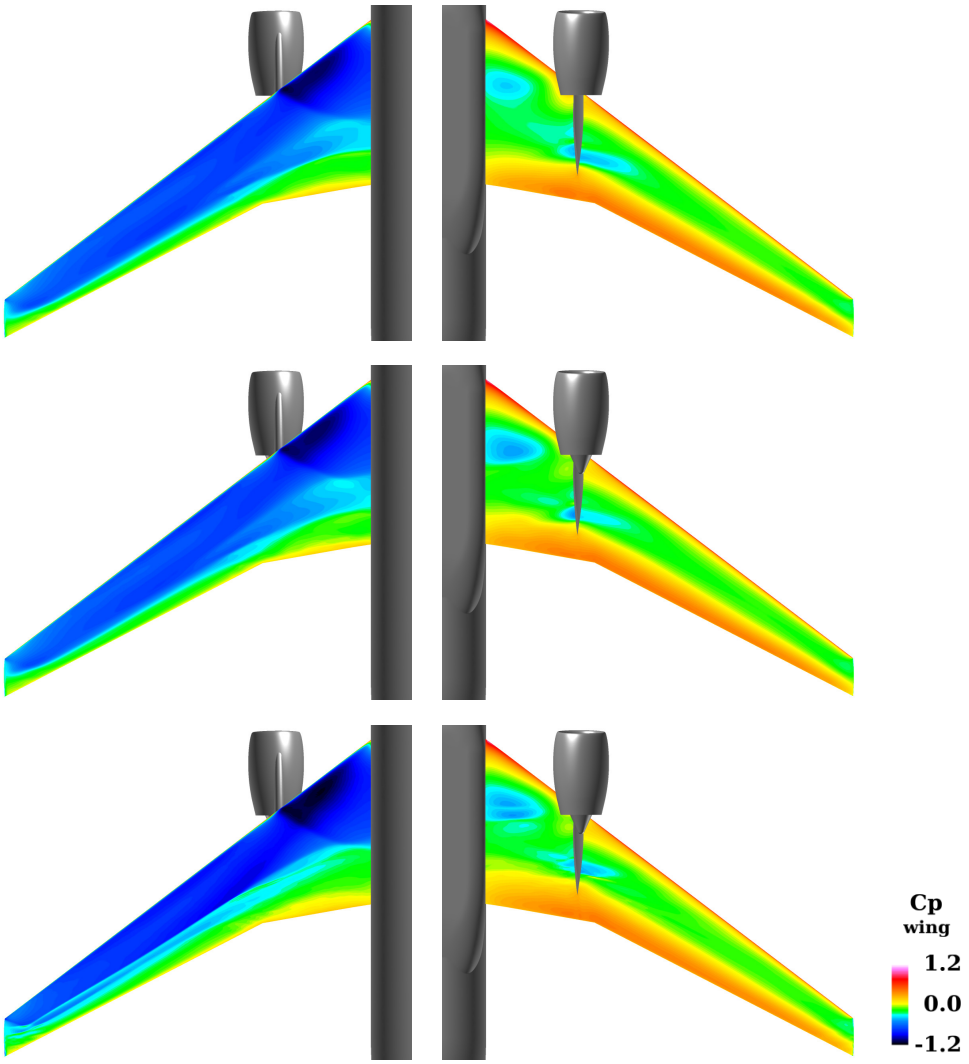


**Figure 9**: Pressure distribution on the wing top side (left and on the wing underside (right). Datasets from top to bottom are flow-through nacelle without slope limiter, integrated simuation without slope limiter and integrated simulation with slope limiter.